The Journal of Chemical Physics

RESEARCH ARTICLE | DECEMBER 15 2025

Computational protocol for emission spectra and PLQY for thermally activated delayed fluorescence derived from sulfur/selenium-incorporated multi-resonant molecules

Special Collection: Yijing Yan Festschrift

Rongrong Li ; Zhigang Shuai

J. Chem. Phys. 163, 234302 (2025)
https://doi.org/10.1063/5.0301546

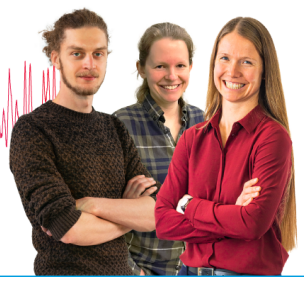

The Journal of Chemical Physics ARTICLE pubs.aip.org/aip/jcp

Computational protocol for emission spectra and PLQY for thermally activated delayed fluorescence derived from sulfur/selenium-incorporated multi-resonant molecules

Cite as: J. Chem. Phys. 163, 234302 (2025); doi: 10.1063/5.0301546
Submitted: 9 September 2025 • Accepted: 25 November 2025 •
Published Online: 15 December 2025

Rongrong Li[1] and Zhigang Shuai[1,2,a)]

AFFILIATIONS

[1] Guangdong Basic Research Center of Excellence for Aggregate Science, School of Science and Engineering, The Chinese University of Hong Kong, Shenzhen, Guangdong 518172, People's Republic of China
[2] MOE Key Laboratory for Organic OptoElectronics and Molecular Engineering, Department of Chemistry, Tsinghua University, Beijing 100084, People's Republic of China

Note: This paper is part of the Special Topic, Yijing Yan Festschrift.
[a)] **Author to whom correspondence should be addressed:** shuaizhigang@cuhk.edu.cn

ABSTRACT

Full width at half maximum (FWHM) is an important indicator for color purity in molecular optical emission. In addition, brightness is determined by photoluminescence quantum efficiency (PLQY). Thermally activated delayed fluorescence (TADF) can convert the electro-pumped triplet states into emissive singlets. Especially, recent experiments suggest that multiple resonance TADF molecules doped with heavy atoms S/Se could effectively avoid the efficiency roll-off by promoting the reverse intersystem crossing (RISC) process. We propose a computational protocol to evaluate FWHM and PLQY based on quantum chemistry calculations and thermal vibration correlation function formalism, which is of great potential to design highly efficient and color-pure molecules. We further build a robust correlation between the reorganization energy of emission state $\lambda^{\mathrm{em}}_{S_1S_0}$ with FWHM and the inverse of reorganization energy of the intersystem crossing (ISC) process $1/\lambda_{S_1T_1}$ with experimental reverse ISC rate constant $k^{\mathrm{exp}}_{\mathrm{RISC}}$, crucial for TADF. Our computational method and findings can be used for the molecular design of organic light-emitting diode materials.

I. INTRODUCTION

Designing and developing highly efficient narrowband emission materials remains a key objective not only for organic light-emitting diodes (OLEDs),[1–4] but also for perovskite,[5,6] quantum dots,[7,8] and phosphors.[9–11] Multi-resonance thermally activated delayed fluorescence (MR-TADF) molecules[12–15] have been found to be especially interesting for achieving narrowband emission and high efficiency. Despite considerable progress, it is still challenging to simultaneously enhance stability, device lifetime, and high color purity.[16] Further development of more environmentally friendly, low-cost materials and manufacturing methods is needed.

MR-TADF molecules, as the next generation of displays, exhibit high efficiency and narrowband emission.[17,18] The long delay lifetime of tens of microseconds leads to severe efficiency roll-off, which hinders their commercial applications. Recently, a series of novel MR-TADF molecules that fuse S/Se atoms into the B-N based frameworks, effectively promoting the reverse intersystem crossing (RISC) process and avoiding efficiency roll-off, are reported.[19–29] The incorporation of heavy atoms enhances spin–orbit coupling (SOC), thereby significantly avoiding efficiency roll-off. However, structural relaxation upon electro- or photoexcitation generally results in a broadened emission spectrum, with full width at half maximum (FWHM) values commonly ranging from 20

Embedding sulfur atoms

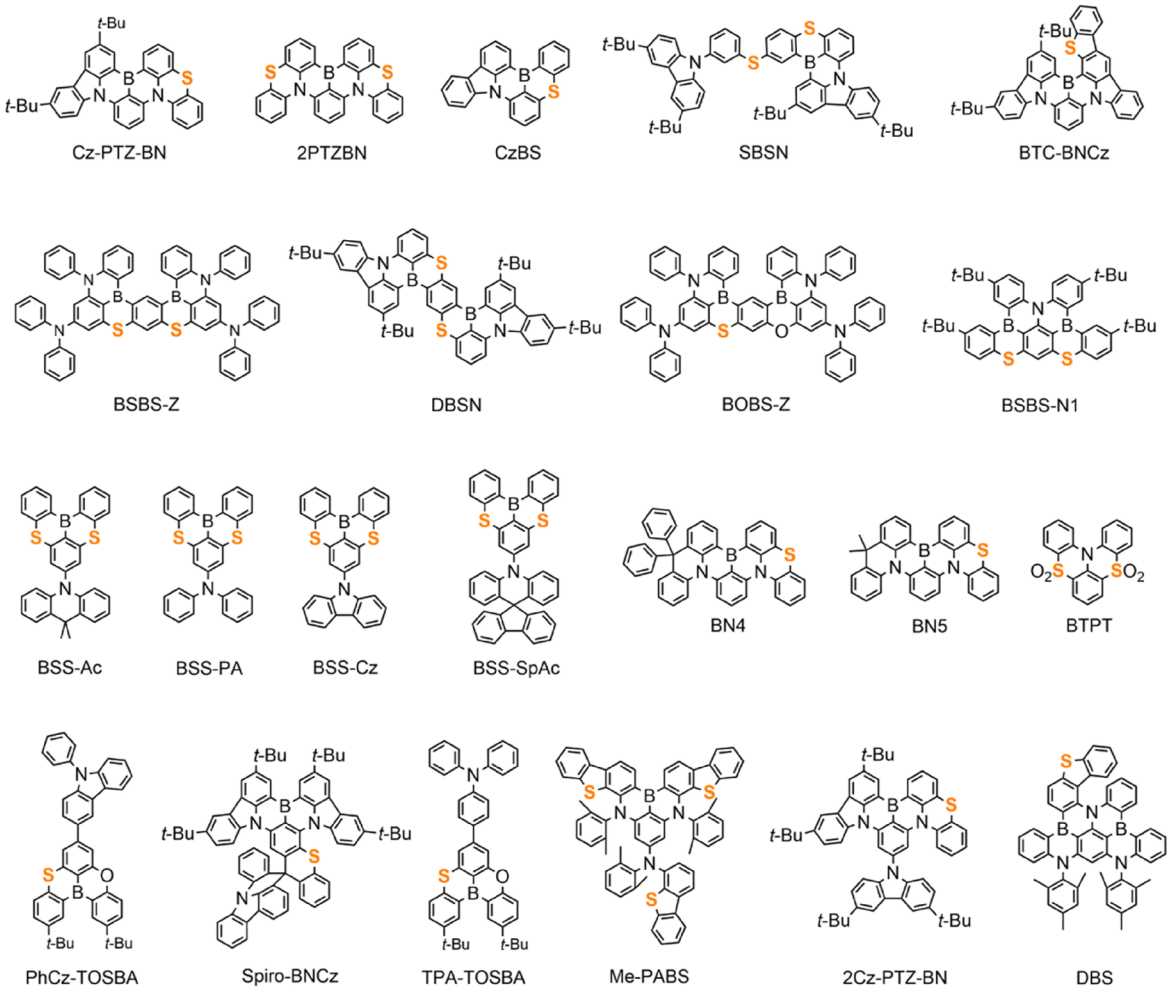

Embedding selenium atoms

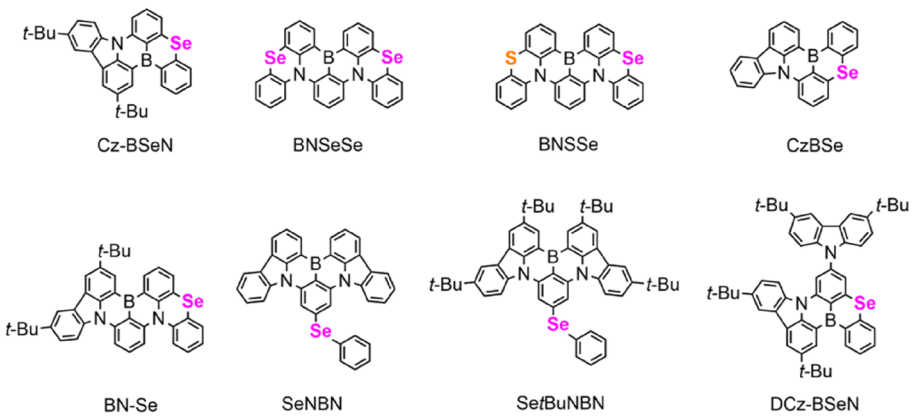

FIG. 1. Chemical structures of literature MR-TADF molecules modeled within this study.

to 100 nm.[30–37] Therefore, reducing FWHM to achieve higher color purity is particularly important for MR-TADF molecules containing heavy atoms.

Since current theoretical methods cannot directly and accurately predict FWHM, different models have been proposed.[38–42] Ahmad *et al.*[38] showed a displaced harmonic oscillator model (DHO), merely using ground state frequency and excited state gradient calculations for the prediction of FWHM. The DHO model is limited within the Franck–Condon approximation and is only suitable for charge transfer or polycyclic aromatic type structures. Furthermore, additional studies involve utilizing the bond order–bond length (BOBL) relationship to correlate variations in bond length or bond order with photophysical properties, thereby improving the performance of organic emissive materials. Wu and co-workers[39] proposed two substitution-driven design strategies to reduce the emission spectrum, according to the contributions of bond length alterations (BLAs) to reorganization energies. Building upon BLA analysis, Troisi and colleagues[40] developed a high-throughput screening approach aimed at identifying organic emission materials exhibiting superior color purity. In 2024, Wang *et al.*[41] reported a simplified one-mode model approximation for FWHM estimation with comparable accuracy to that of all vibrational modes model. Nevertheless, most of the existing investigations center on polycyclic aromatic hydrocarbons or a restricted number of conventional TADF systems, limiting their applicability to the recently developed MR-TADF molecules.

In this study, we propose a computational scheme to evaluate FWHM and photoluminescence quantum efficiency (PLQY) and to perform systematic computational simulations on a series of MR-TADF molecules containing chalcogen atoms (S/Se). Figure 1 shows the chemical structures of modeled molecules.[19–37] Combining the quantum chemistry packages and thermal vibrational correlation function (TVCF) we developed earlier as implemented in the home-built MOMAP program,[43–45] we found that B3LYP or PBE0 calculated excited energy based on the optimized electronic structure from the CAM-B3LYP exhibits reasonable FWHM values with mean absolute error (MAE) ~ 8 nm. A convincing linear relationship (R^2 = 0.844) between FWHM and reorganization energy $\lambda^{\mathrm{em}}_{S_1S_0}$ enables a robust and explicit judgment of color purity for these MR-TADF molecules. The TVCF combined with CAM-B3LYP optimized electronic structure yields the best prediction for PLQY with a MAE of 26%. The main error contribution originates from the non-radiative rate constants (k_{IC}) calculation. Furthermore, we plot the experimental RISC rate constant $k^{\mathrm{exp}}_{\mathrm{RISC}}$ with respect to $1/\lambda^{\mathrm{em}}_{S_1T_1}$. Although the linear fitting coefficient R^2 = 0.700 is not ideal, it still helps rapidly and qualitatively compare RISC rates of different molecules.

II. METHODOLOGY

We employ the Gaussian 16 program[46] to perform all the quantum chemistry calculations. Each of the singlet ground (S_0) and excited state (S_1) geometries of the 30 MR-TADF molecules are optimized using five functionals, including PBE0,[47] TPSSh,[48] ωB97X-D,[49] and B3LYP[50] in combination with the third version of Grimme's atom pairwise dispersion corrections with Becke–Johnson damping (D3BJ)[51,52] and CAM-B3LYP[53]-D3BJ for density functional theory (DFT) and time-dependent DFT (TDDFT), respectively. The geometries of the triplet states (T_1) are optimized using three functionals, PBE0, B3LYP-D3BJ, and CAM-B3LYP-D3BJ, under unrestricted open-shell DFT levels. Unless otherwise noted, the geometry optimization and frequency analysis use the 6-31G(d) basis set.[54,55] All calculations employ the linear-response polarizable continuum model (LR-PCM) with the solvation model based on density (SMD), using toluene (ε = 2.37) as the solvent in accordance with the experimental conditions.[56,57] Geometry optimizations use equilibrium solvation, whereas vertical absorption and emission energies are evaluated under the non-equilibrium solvation treatment.

All the rate constants and emission spectrum calculations are based on the TVCF formalism we developed and implemented in a home-built and commercially available package, MOMAP. The TVCF method transforms the line shape function $L(\omega)$ into the time domain correlation function χ. The correlation function χ possessing a known analytical expression can be expressed in terms of the partition function Z_{vib} and the vibrational Hamiltonians H_{i} and H_{f} for the initial and final states. Therefore, the TVCF method effectively avoids the truncation errors of the sum-of-states method. The calculation formula is as follows:

$$L(\omega) = \frac{1}{2\pi}\int \omega^3 e^{-it(\Delta E_{ad}/\hbar-\omega)}\chi(t,T)dt, \tag{1}$$

$$\chi(t,T) = Z_{\mathrm{vib}}^{-1}\,\mathrm{Tr}\left(e^{(i\hat{H}_{\mathrm{i}}/\hbar-\beta\hat{H}_{\mathrm{i}})t}e^{-i\hat{H}_{\mathrm{f}}t/\hbar}\right), \tag{2}$$

where ω is the frequency of the ith normal mode, the ΔE_{ad} is the adiabatic excitation energy, and T is the temperature, which is set to 300 K in this study; $\hat{H}_{\mathrm{f}}$ and $\hat{H}_{\mathrm{i}}$ are the harmonic oscillator Hamiltonians of the final and initial electronic states, respectively, and β is the reciprocal of temperature T times Boltzmann constant k_B. Unless otherwise specified, the Adiabatic Hessian (AH) model with linear Duschinsky relation and Cartesian coordinates is used for all calculations. A Lorentzian-type broadening with 100 cm^{-1} FWHM is applied to all investigated systems in the calculation of emission spectra and radiation rate constant (k_{R}), and the Herzberg–Teller (HT) effect is not considered in all calculations. The calculation of k_{R} is to integrate the emission spectrum,

$$k_{\mathrm{R}}(T) = \int \sigma_{\mathrm{em}}(\omega,T)d\omega, \tag{3}$$

$$\sigma_{em}(\omega,T) = \frac{2\omega^3}{3\pi\hbar c^3}|\mu_{\mathrm{fi}}|^2\int_{-\infty}^{+\infty} e^{-i(\omega-\omega_{\mathrm{if}})t}\rho_{\mathrm{em}}(t,T)dt, \tag{4}$$

where $\sigma_{\mathrm{em}}(\omega,T)$ is the emission spectrum, μ_{fi} is the electric transition dipole moment between the final and initial electronic states, $\rho_{\mathrm{em}}(t,T) = Z_{\mathrm{i}}^{-1}\,\mathrm{Tr}\left(e^{-i\tau_{\mathrm{f}}\hat{H}_{\mathrm{f}}}e^{-i\tau_{\mathrm{i}}\hat{H}_{\mathrm{i}}}\right)$ is the TVCFs, and $\tau = t/\hbar$. The nonradiative rate constant k_{IC} between the two electronic states within the same spin manifold can be expressed as

$$k_{\mathrm{IC}} = \frac{1}{\hbar^2}\sum_{kl}\mathrm{R}_{kl}\int_{-\infty}^{+\infty} e^{i\omega_{\mathrm{if}}t}\rho^{\mathrm{IC}}_{\mathrm{fi,kl}}(t,T)dt, \tag{5}$$

where R_{kl} is the non-adiabatic coupling matrix between two electronic states Φ_{f} and Φ_{i}, $\mathrm{R}_{kl} = \langle\Phi_{\mathrm{f}}|\hat{P}_{fk}|\Phi_{\mathrm{i}}\rangle\langle\Phi_{\mathrm{i}}|\hat{P}_{fl}|\Phi_{\mathrm{f}}\rangle$, $\hat{P}_{fk}$ and $\hat{P}_{fl}$ are the nuclear momentum operators for the corresponding vibrational normal mode, $\hat{P} = -i\hbar\frac{\delta}{\delta Q}$, Q is the vibration normal mode

coordinate, $\rho_{\mathrm{fi,kl}}^{\mathrm{IC}}(t,T) = Z_{\mathrm{i}}^{-1}\,\mathrm{Tr}\,(\hat{P}_{\mathrm{fk}}e^{-i\tau_{\mathrm{f}}\hat{H}_{\mathrm{f}}}e^{-i\tau_{\mathrm{i}}\hat{H}_{\mathrm{i}}})$ is the internal conversion correlation function, and $Z_{\mathrm{i}} = \sum_{v=0}^{\infty} e^{-\beta E_{iv}}$ is the partition function for the vibrational normal mode. Non-adiabatic coupling calculations are performed using the NACME module in MOMAP, employing transition electric fields and vibrational information from Gaussian output. The adiabatic excitation energy ΔE_{ad} is calculated by subtracting the S_0 energy obtained from DFT from the S_1 energy obtained from TDDFT. For the intersystem crossing (ISC) and RISC processes with electron spin changes between singlet and triplet states, the corresponding rate constant should be expressed as

$$k_{\mathrm{ISC/RISC}} = \frac{1}{\hbar^2}\left|\langle\Phi_{\mathrm{f}}|\hat{H}^{\mathrm{SO}}|\Phi_{\mathrm{i}}\rangle\right|^2 \int_{-\infty}^{+\infty} e^{i\omega_{\mathrm{if}}t}\rho_{\mathrm{fi}}^{\mathrm{ISC/RISC}}(t,T)dt, \quad (6)$$

where $\left|\langle\Phi_{\mathrm{f}}|\hat{H}^{\mathrm{SO}}|\Phi_{\mathrm{i}}\rangle\right|$ is the spin–orbit coupling (SOC) term and $\rho_{\mathrm{fi}}^{\mathrm{isc/risc}}(t,T) = Z_{\mathrm{i}}^{-1}\,\mathrm{Tr}\,(e^{-i\tau_{\mathrm{f}}\hat{H}_{\mathrm{f}}}e^{-i\tau_{\mathrm{i}}\hat{H}_{\mathrm{i}}})$ is the ISC/RISC correlation function. The electronic structure information required for the theoretical formulations of MOMAP is obtained within the framework of density functional theory and time-dependent density functional theory. For the calculation of the ISC rate constant k_{ISC} and RISC rate constant k_{RISC}, SOC is evaluated at the CAM-B3LYP-D3/6-31G(d) level for S_1 and T_1 optimized geometry, respectively, in the Q-Chem 5.3 program.[58] The significant contribution of double excitations of MR-TADF systems makes the TDDFT method no longer suitable for calculating their singlet–triplet energy gap ΔE_{ST}. Therefore, based on the same S_1 electronic structures with SOC calculations, a high-level wave function SCS-CC2[59] method with a def2-TZVP[60,61] basis set is applied to calculate the ΔE_{ST}.

III. RESULTS AND DISCUSSION

A. Benchmarking of investigated MR-TADF molecules

The accuracy of photophysical property calculations depends on the input electronic structure information. To identify a reliable function for evaluating the electronic structure information, we used five different density functions with different percentages of Hartree–Fock exact exchanges to calculate the maximum absorption (λ_{abs}) and emission wavelength (λ_{em}) of 30 MR-TADF molecules doped with sulfur or selenium atoms. Figure 2(a) displays the MAE of λ_{abs} and λ_{em} compared with experimental values. Figures 2(b)–2(f) show the experimental λ_{em} vs that of five functionals, PBE0, TPSSh, ωB97X-D, B3LYP-D3BJ, and CAM-B3LYP-D3BJ, and the calculated values for each molecule, respectively. Both λ_{abs} and λ_{em} are directly obtained from the vertical TDDFT calculation based on the corresponding optimized S_0 and S_1 structures. The explicit numbers of experimental and TDDFT calculated λ_{abs} and λ_{em} are listed in Tables S1 and S2 in the supplementary material, respectively.

Among the five functionals, the MAE trend of the same functional is consistent for the absorption and emission. B3LYP

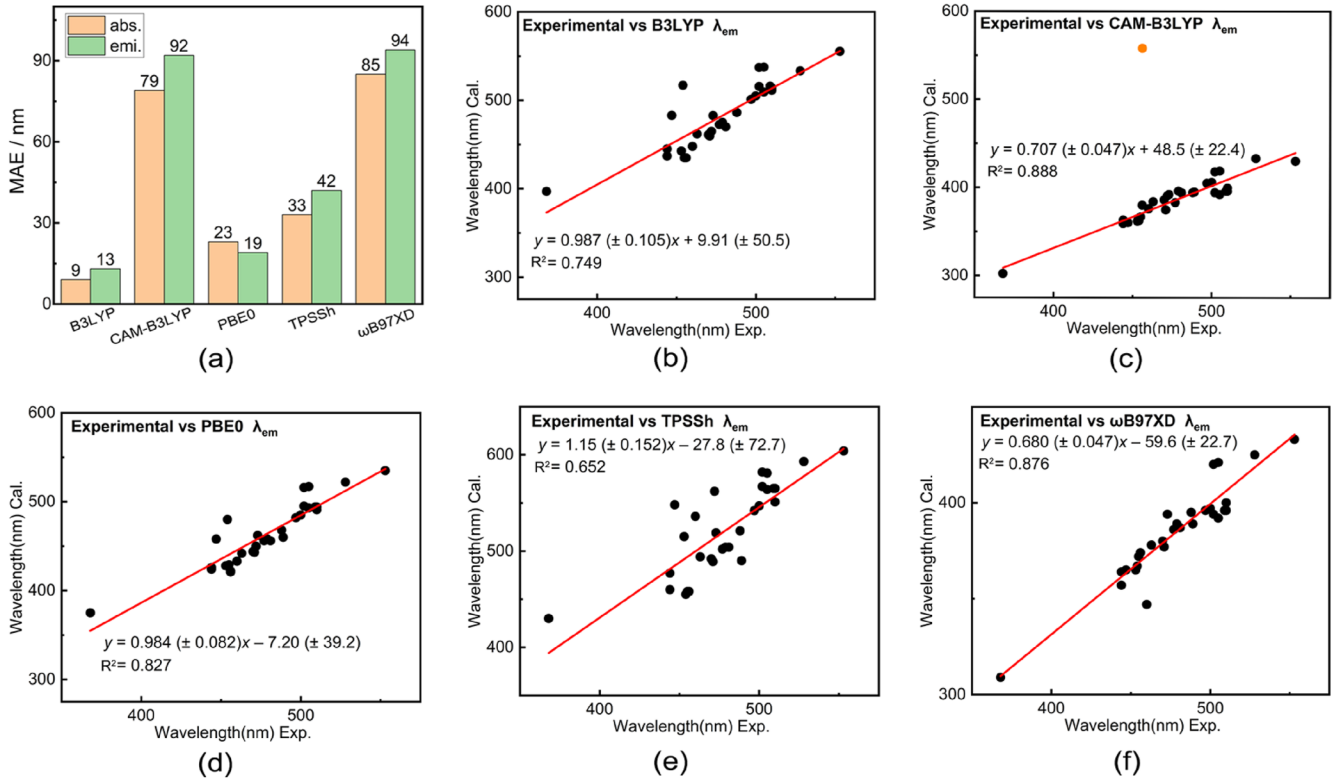

FIG. 2. MAE of different functionals calculated maximum absorption and emission wavelengths with respect to the experiment (a). The experimental vs different functionals calculated maximum emission wavelength (b)–(f). The fitting excluded the obviously incorrect orange data points in panel (c).

characterizes the smallest MAE for both absorption and emission wavelengths. While the MAE for CAM-B3LYP and ωB97X-D is relatively large, ranging from 79 to 94 nm. Generally, range-separated functionals can accurately describe charge-transfer excited states. However, since the S_1 state of MR-TADF molecules is a multiple-resonance state, it is reasonable that these two long-range corrected functionals exhibit relatively large computational errors. Except for TPSSh, other functionals all have a better linear correlation between the experimentally determined and calculated maximum emission wavelength. The correlation of TPSSh is modest with a 0.652 R^2 value. The qualitative prediction of maximum emission wavelength using TDDFT methods for such molecules is reliable. Although the MAE is large, CAM-B3LYP features the best correlation with R^2 of 0.888. Comprehensively considering the MAE and linear correlation, we further evaluated the photophysical properties based on B3LYP, CAM-B3LYP, and PBE0 calculated electronic structures.

B. The evaluation of FWHM

Table I displays the FWHM for different functionals combined with TVCF methods. The calculated FWHM values align more closely with experimental data without Duschinsky rotation. Therefore, the displaced harmonic oscillator with different frequencies (DODF) model is used in this section. Indeed, Chen *et al.* have reported that the DODF model, which neglects Duschinsky rotation, performs better in the prediction of phosphorescence spectra.[62] B3LYP (or PBE0/CAM-B3LYP) means that both the electronic structure information and the adiabatic excitation energies (E_{ad}) are obtained using the B3LYP (or PBE0/CAM-B3LYP) functional. CAM-B3LYP/B3LYP indicates that the electronic structure information required for calculations in Eqs. (1) and (2) is derived from CAM-B3LYP, while the adiabatic excitation energy is computed using B3LYP based on the S_0 and S_1 geometries optimized with CAM-B3LYP. Similarly, CAM-B3LYP/PBE0 follows the same convention. As we can see, the MAE of FWHM directly calculated by B3LYP, PBE0, and CAM-B3LYP is large with values of 12, 11, and 13 nm, respectively. The FWHM values obtained with CAM-B3LYP are significantly smaller than those with B3LYP. This is because the adiabatic excitation energy calculated by CAM-B3LYP is larger than that by B3LYP, and according to Eq. (1), the FWHM value with CAM-B3LYP should indeed be smaller. The FWHM of most of these molecules ranges from 20 to 40 nm. The deviations around 12 nm are nearly 1/2 to 1/3 the experiments and are clearly unreasonable. The accuracy is improved effectively, with the MAE of both CAM-B3LYP/B3LYP and CAM-B3LYP/PBE0 decreased to 8 nm,

TABLE I. Experimental and TVCF combined with different functionals calculated FWHM (nm) for S/Se-incorporated MR-TADF molecules.

Molecule	Exp.	B3LYP	PBE0	CAM -B3LYP	CAM-B3LYP /B3LYP	CAM-B3LYP /PBE0
Cz-PTZ-BN	37	58	54	23	34	32
2Cz-PTZ-BN	38	64	63	24	36	33
BOBS-Z	21	20	26	13	19	18
BSBS-Z	20	49	46	29	42	39
BSBS-N1	21	27	24	14	20	18
2PTZBN	39	45	42	25	38	35
SBSN	27	—	23	16	31	29
DBSN	28	23	22	19	29	27
BSS-PA	35	41	36	25	35	33
BSS-Cz	28	—	21	17	23	22
BN-Se	42	64	59	22	34	31
BTPT	33	58	48	17	24	22
PhCz-TOSBA	32	21	20	16	22	21
TPA-TOSBA	34	31	49	17	25	23
CzBS	28	19	18	12	17	15
CzBSe	33	20	20	15	21	20
BNSSe	39	58	54	35	54	50
BNSeSe	38	58	54	35	54	50
Spiro-BNCz	42	54	—	32	47	45
BTC-BNCz	23	11	11	7	10	9
Me-PABS	21	22	18	15	21	20
BN4	43	42	41	22	33	31
BN5	44	41	40	22	33	31
Cz-BSeN	30	19	19	14	19	18
DB-S	23	26	—	9	13	12
MAE		12	11	13	8	8
R^2		0.402	0.467	0.344	0.369	0.371

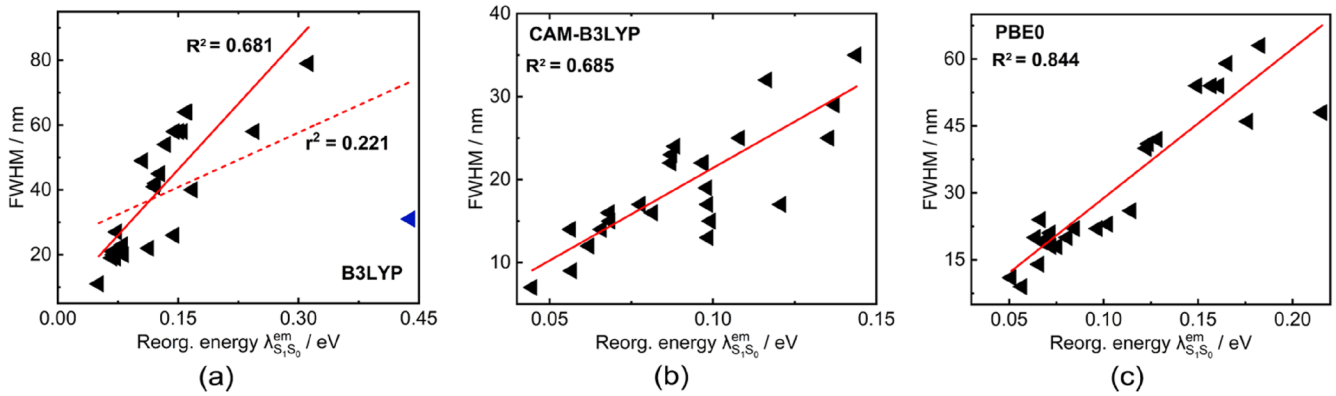

FIG. 3. Correlation between S_1 emission reorganization energy ($\lambda^{em}_{S_1S_0}$) and emission FWHM calculated by three different functionals: B3LYP (a), CAM-B3LYP (b), and PBE0 (c). In panel (a), the red solid line is the fitted trend line after excluding the blue data points, while the red dashed line is the fitted line including all data points.

indicating a reliable calculated result. The absorption and emission spectrum of all 29 molecules calculated by the TVCF method combined with CAM-B3LYP/B3LYP and the explicit numbers of λ_{em} calculated by TVCF with CAM-B3LYP are shown in Fig. S1 and Table S2 in the supplementary material, respectively. TVCF shows good evaluation performance for maximum emission wavelengths, with a MAE of only 12 nm compared to experimental values. While two molecules, SeNBN and SetBuNBN, are given incorrect spectra that violate experiment data, indicating problematic results of electronic structure calculations, so the corresponding FWHM values are not included in Table I. The unphysical spectra (too broad) of DCz-BSeN, which may be due to the inapplicability of the harmonic oscillator approximation, are also not included in Fig. S1 and Table I. However, the FWHM correlation between all five calculation schemes and the experiment is poor, and all R^2 values are less than 0.5.

Under the harmonic oscillator approximation, the total reorganization energy of the system can be evaluated through normal mode analysis, as shown below:

$$\lambda = \sum_i \frac{1}{2}\omega_i^2 \Delta Q_i^2, \tag{7}$$

where ω_i is the frequency of the ith normal mode, and ΔQ_i is the displacement along the ith normal mode coordinate between S_0 and S_1. EVC calculation in MOMAP directly provides the reorganization energy and Huang–Rhys factors based on the output from the quantum chemistry programs (Gaussian in this study). The correlations between S_1 emission reorganization energy ($\lambda^{em}_{S_1S_0}$) and corresponding FWHM evaluated by three functionals are plotted in Figs. 3(a)–3(c), respectively. The explicit numbers of $\lambda^{em}_{S_1S_0}$ are listed in Table S3 in the supplementary material. The emission reorganization energy of all three functionals possesses better linear correlations, and PBE0 has the best performance with an R^2 value of 0.844. Although the R^2 values of B3LYP and CAM-B3LYP are poorer than those of PBE0, they are close to 0.7, which is enough for qualitative comparisons. Therefore, we consider the use of reorganization energy $\lambda^{em}_{S_1S_0}$ to qualitatively assess the FWHM to be functional-insensitive. Furthermore, the reorganization energy calculation based on electron–vibration coupling is very fast and has low computational consumption. Therefore, $\lambda^{em}_{S_1S_0}$ as the descriptor to qualitatively predict FWHM is convincing. Based on the linear relationship between $\lambda^{em}_{S_1S_0}$ and the FWHM calculated by B3LYP, when $\lambda^{em}_{S_1S_0}$ is less than 0.124 and 0.053 eV, the FWHM is correspondingly less than 39 and 20 nm.

C. The evaluation of PLQY

The calculated PLQY and different photophysical properties are shown in Table II. The explicit numbers for ΔE_{ST} from both experiments and SCS-CC2 calculations are provided in Table S4 of the supplementary material. The calculation results of SCS-CC2 for ΔE_{ST} are excellent, yielding a MAE of only 0.043 eV compared to experimental values. We also attempt three functionals for PLQY evaluation, and CAM-B3LYP showed the best accuracy with an error of 26%. By comparing the rate constants of different photophysical processes, we found that the error in PLQY prediction for these molecules mainly came from the evaluation of k_{IC}. The calculation deviation for k_R and k_{ISC} is generally within 1 to 2 orders of magnitude, while the deviation for k_{IC} reaches 2 to 3 orders of magnitude. Furthermore, k_{IC} vs adiabatic excitation energies E_{ad} is plotted in Fig. S2 in the supplementary material. As we can see, k_{IC} decreases with increasing E_{ad}, in accordance with the energy gap law. The large errors of the internal conversion process may be introduced by the harmonic oscillator approximation.[63,64] The k_R, k_{IC}, and k_{ISC} computed with B3LYP and PBE0, along with experimental data, are listed in Tables S5–S7 in the supplementary material, respectively.

D. The correlation between $\lambda_{S_1T_1}$ and k^{exp}_{RISC}

The k_{RISC} also has large deviations from the experimental values, as shown in Table S8. According to the Marcus–Levich–Jortner theory,

$$k_{RISC} = \frac{2\pi}{\hbar} V_{SOC}^2 \frac{1}{\sqrt{4\pi\lambda_M k_B T}} \sum_{n=0}^{\infty} \exp(-S)\frac{S^n}{n!} \times \exp\left[-\frac{(\Delta E_{ST} + n\hbar\omega_{eff} + \lambda_M)^2}{4\lambda_M k_B T}\right], \tag{8}$$

TABLE II. Experimental and calculated PLQY (%) and photophysical properties based on CAM-B3LYP optimized structures.

Molecule	PLQY (%) Exp.	PLQY (%) CAM -B3LYP[a]	k_R ($\times 10^8$ s^{-1})	k_{IC} (s^{-1})	k_{ISC} ($\times 10^8$ s^{-1})	SOC (cm^{-1})	ΔE_{ST} (eV)
Cz-PTZ-BN	84	86	1.89	3.50×10^3	2.95×10^7	2.27	0.11
2Cz-PTZ-BN	87	77	1.78	1.52×10^7	3.79×10^7	0.370	0.09
BSBS-N1	59	23	2.23	2.61×10^4	7.43×10^8	0.995	0.06
SBSN	76	50	1.49	8.24×10^7	6.75×10^7	0.367	0.10
DBSN	98	71	1.78	7.37×10^7	6.89×10^4	0.016	0.15
BSS-Ac	90	34	0.889	2.49×10^2	1.72×10^8	1.11	0.17
BSS-SpAc	89	28	0.905	7.84×10	2.29×10^8	1.12	0.17
BN-Se	99	68	1.97	2.57×10^3	9.16×10^7	0.381	0.08
PhCz-TOSBA	39	50	0.980	2.76×10^3	9.76×10^7	0.835	0.16
BNSSe	99	90	1.11	2.26×10^4	1.29×10^7	0.210	0.10
BNSeSe	100	92	1.21	2.41×10^4	1.05×10^7	0.174	0.10
DB-S	95	84	1.48	1.42×10^4	2.74×10^7	1.19	0.13
Cz-BSeN	87	35	1.77	1.64×10^3	3.31×10^8	2.27	0.13

[a]Theoretical PLQY is evaluated via $\Phi = k_R/(k_R + k_{IC} + k_{ISC})$.

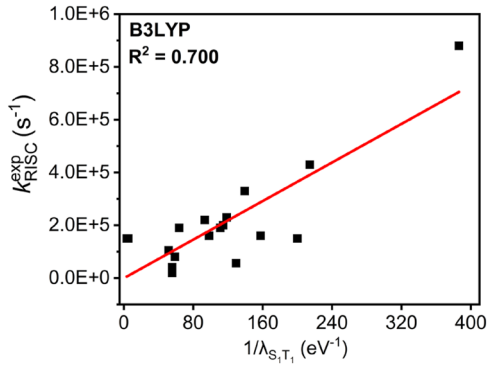

FIG. 4. Experimental RISC rate constant k_{RISC}^{exp} with respect to calculated the $1/\lambda_{S_1T_1}$.

where λ_M is the reorganization energy, S is the Huang–Rhys factor, $\hbar\omega_{eff}$ is the effective energy, k_B is Boltzmann's constant, and T is temperature. We plotted the experimental RISC rate constant k_{RISC}^{exp} with respect to the calculated $1/\lambda_{S_1T_1}$, as shown in Fig. 4. The linear fitting coefficient R^2 is 0.700, indicating a better correlation between experimental k_{RISC}^{exp} and theoretically computed $1/\lambda_{S_1T_1}$. It demonstrates that the reciprocal reorganization energy $\lambda_{S_1T_1}$ to qualitatively compare the RISC rates of MR-TADF molecules containing heavy atoms is reasonable. When $1/\lambda_{S_1T_1}$ calculated by B3LYP is larger than 44 eV^{-1}, k_{RISC} is accordingly greater than 10^5 s^{-1}. The $\lambda_{S_1T_1}$ values in Fig. 4 are displayed in Table S9.

Figure 5(a) summarizes the computed reorganization energy $\lambda_{S_1S_0}^{em}$ and $1/\lambda_{S_1T_1}$ to predict the FWHM and k_{RISC}, respectively. Both experiment and calculation indicate that BSBS-Z and BTC-BNCz perform narrowband emission and fast RISC rate. Subsequently, we analyzed the vibrational coupling constants and emission spectra of the S_1 states of these two molecules, as shown in Figs. 5(b)–5(e). The Huang–Rhys factors of high-frequency vibrational modes for both BSBS-Z and BTC-BNCz are very small. For BSBS-Z, the vibrational modes with large Huang–Rhys factors (>0.5) focus on the low-frequency (<25 cm^{-1}). The Huang–Rhys factors of all vibrational modes are less than 0.25 for BTC-BNCz, so the emission spectrum is also very narrow.

Convinced by our reasonable predictions of FWHM and k_{RISC} through reorganization energies, we can now design a series of MR-TADF molecules with similar structures to BSBS-Z and BTC-BNCz, which are further optimized by embedding sulfur and selenium atoms. The geometry structures and computed reorganization energy $\lambda_{S_1S_0}^{em}$ of designed molecules are displayed in Figs. 5(f) and 6, respectively. Since the significant improvement of both RISC and efficiency roll-off in heavy atom doped molecules reported by experiment, we did not further calculate $\lambda_{S_1T_1}$ to evaluate the k_{RISC}. In addition, the molecules with $\lambda_{S_1S_0}^{em}$ larger than 0.620 eV (5000 cm^{-1}) are excluded. As we can see, five molecules, B2-Se, BNCz-S, DB′-Se, *t*-BuCz-DABNA-S, and *t*-BuCz-DABNA-Se with small $\lambda_{S_1S_0}^{em}$ (<0.053 eV), characterize narrow FWHM less than 20 nm. The emission reorganization energy of B2-S, BNCz-Se, and DB′-S is 0.064, 0.058, and 0.054 eV, respectively, also corresponding to narrowband emission. While the FWHM of the parent molecule, Π-CzBN, is 16 nm, the FWHM of S/Se doped Π-CzBN derivatives significantly increases. It indicates that the heavy atom effect improves efficiency roll-off while increasing FWHM, which is unfavorable. For the body structure of ADBNA-Me, doped with a Se atom, it is better than with an S atom. The large conjugated systems, such as m-*v*-DABNA-S and Π-CzBN-S/Se, are not suitable for embedding heavy atoms due to broadening FWHM. The explicit number of reorganization energy $\lambda_{S_1S_0}^{em}$ for virtually designed MR-TADF molecules is shown in Table S10 in the supplementary material.

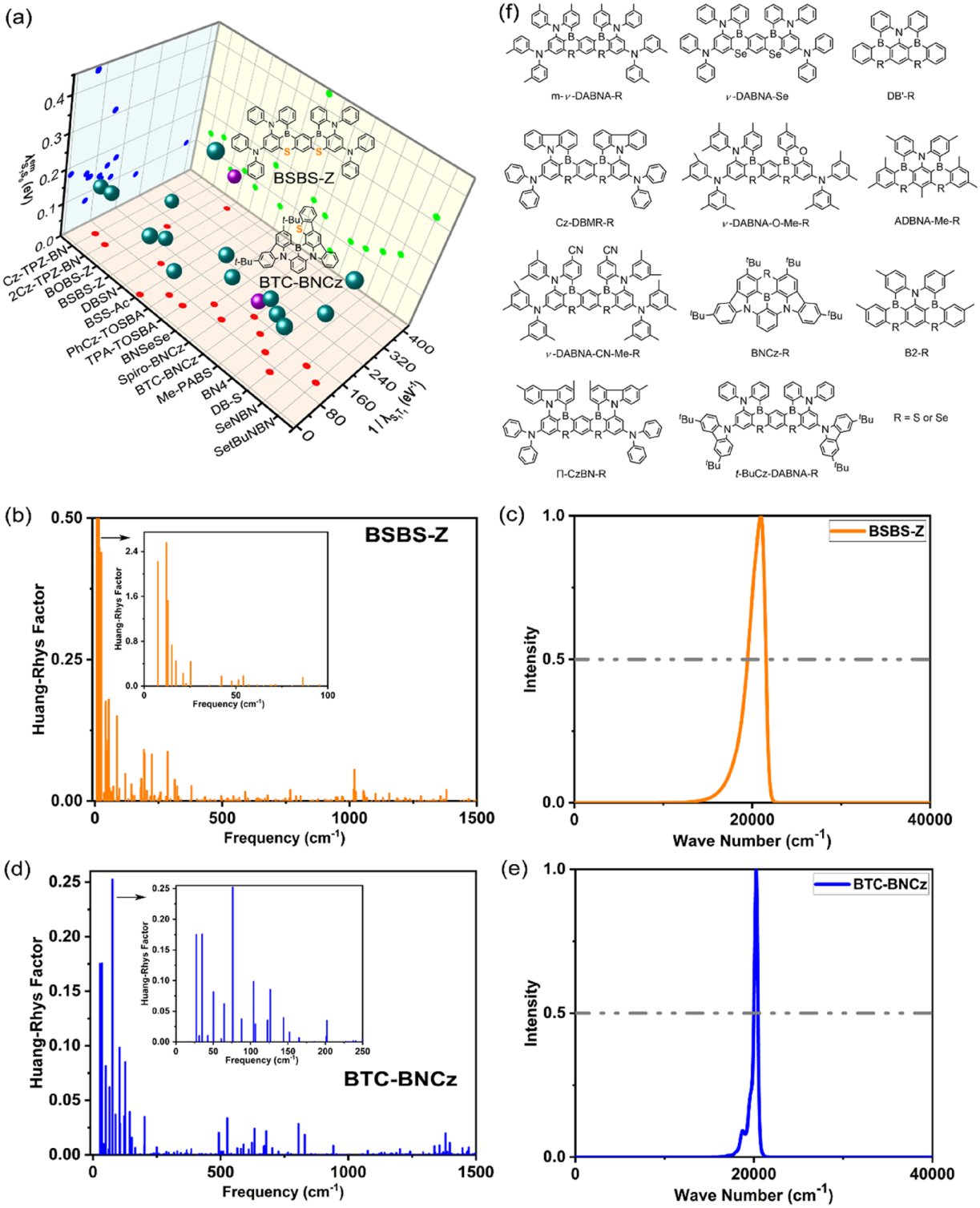

FIG. 5. Reorganization energy $\lambda^{em}_{S_1S_0}$ and $1/\lambda_{S_1T_1}$ for 16 experimental MR-TADF molecules (a). Histogram of vibrational coupling constants (Huang–Rhys factors) based on S_1 normal modes for BSBS-Z (b) and BTC-BNCz (d). Normalized vibronic fluorescent emissive spectra of BSBS-Z (c) and BTC-BNCz (e). Virtually designed MR-TADF molecules containing heavy atoms (f).

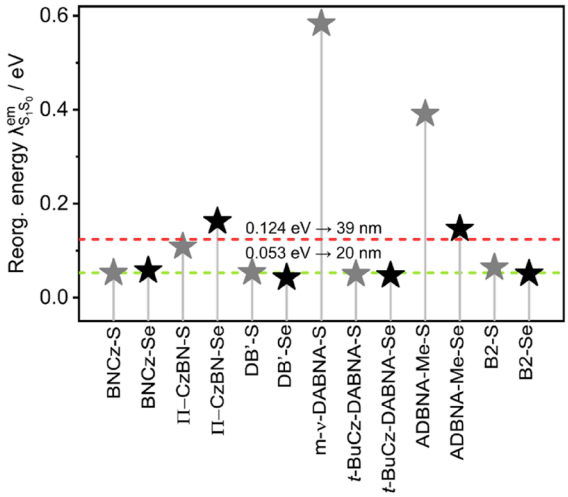

FIG. 6. Emission reorganization energy of 13 MR-TADF molecules with predicted narrowband emission. The green dashed line and red dashed line represent FWHM less than 20 and 39 nm, respectively.

IV. CONCLUSION

In summary, we established a robust computational scheme for qualitative and quantitative prediction of FWHM based on systematic simulation of photophysical properties of 30 novel MR-TADF molecules containing S/Se atoms by DFT/TDDFT, SCS-CC2, and TVCF rate formalism. It is found that $\lambda^{em}_{S_1S_0}$ as a good descriptor for FWHM is quite robust, almost independent of the choice of functionals. CAM-B3LYP achieves a relatively good accuracy in calculating the PLQY of these molecules with an error of ~26%, which mostly stems from the evaluation of the non-radiative rate constant, a very challenging issue. The moderate linear correlation (R^2 = 0.700) between $1/\lambda_{S_1T_1}$ and k^{exp}_{RISC} can be employed for a quick and qualitatively correct prediction of RISC rate. Five virtually designed molecules, B2-Se, BNCz-S, DB′-Se, *t*-BuCz-DABNA-S, and *t*-BuCz-DABNA-Se, show a narrow FWHM of less than 20 nm. Given the challenge of color purity for OLEDs, we believe the theoretical investigations presented in this study can serve as guidance to both theoretical and experimental research in the future.

SUPPLEMENTARY MATERIAL

The explicit numbers of experimental and calculated maximum absorption and emission wavelengths, absorption and emission spectra, emission reorganization energy, and singlet–triplet energy gaps, as well as photophysical properties, are available in the supplementary material.

ACKNOWLEDGMENTS

Z.S. has been inspired by the achievements of Professor Yijing Yan. Especially, the TVCF formalism employed in this study has followed him and been stimulated by him. We take this opportunity of celebrating Yijing Yan's 70th birthday to express our deepest gratitude and sincerest wishes. This study is supported by the National Natural Science Foundation of China (Grant Nos. T2350009 and 22433007), the Guangdong Provincial Natural Science Foundation (Grant No. 2024A1515011185), and the Shenzhen City Peacock Team Project (Grant No. KQTD20240729102028011). R.L. and Z.S. are supported by the Guangdong Basic Research Center of Excellence for Aggregate Science.

AUTHOR DECLARATIONS

Conflict of Interest

The authors have no conflicts to disclose.

Author Contributions

Rongrong Li: Conceptualization (equal); Data curation (equal); Formal analysis (equal); Investigation (equal); Methodology (equal); Validation (equal); Visualization (equal); Writing – original draft (equal); Writing – review & editing (equal). **Zhigang Shuai**: Conceptualization (equal); Data curation (equal); Formal analysis (equal); Funding acquisition (lead); Investigation (equal); Methodology (equal); Project administration (lead); Resources (lead); Software (lead); Supervision (lead); Validation (equal); Visualization (equal); Writing – review & editing (equal).

DATA AVAILABILITY

The data that support the findings of this study are available within the article and its supplementary material.

REFERENCES

[1] P. Liu, X. Y. Tang, C. Z. Du, R. Xue, X. Y. Chen, J. Cao, and X. Y. Wang, "Lighting up nonbenzenoid acepleiadylene with ultra-narrowband emission through aromaticity modulation," Sci. China Chem. **66**(12), 3506–3510 (2023).
[2] Y. Feng, Y. Xu, C. Qu, Q. Wang, K. Ye, Y. Liu, and Y. Wang, "Structurally tunable donor–bridge–fluorophore architecture enables highly efficient and concentration-independent narrowband electroluminescence," Adv. Mater. **36**(31), 2403061 (2024).
[3] J. M. Ha, S. H. Hur, A. Pathak, J. E. Jeong, and H. Y. Woo, "Recent advances in organic luminescent materials with narrowband emission," NPG Asia Mater. **13**, 53 (2021).
[4] S. Jiang, D. Liu, Z. Chen, Z. Yang, Y. He, G. X. Yang, D. Li, and S. J. Su, "Carbonyl-based narrowband emitters peripherally decorated by sulfone-containing spiro structures," Adv. Funct. Mater. **34**(32), 2316355 (2024).
[5] J. N. Yang, T. Chen, J. Ge, J. J. Wang, Y. C. Yin, Y. F. Lan, X. C. Ru, Z. Y. Ma, Q. Zhang, and H. B. Yao, "High color purity and efficient green light-emitting diode using perovskite nanocrystals with the size overly exceeding bohr exciton diameter," J. Am. Chem. Soc. **143**(47), 19928–19937 (2021).
[6] L. Li, Y. Hu, Y. Chen, C. Wang, G. Zhao, X. Du, C. Wang, L. Xiao, Z. Lu, J. Wang, D. Wang, J. Jie, J. Huang, and G. Zou, "Surface defect suppression for high color purity light-emitting diode of free-standing single-crystal perovskite film," Adv. Funct. Mater. **33**(29), 2301205 (2023).
[7] Y. Bi, S. Cao, P. Yu, Z. Du, Y. Wang, J. Zheng, B. Zou, and J. Zhao, "Reducing emission linewidth of pure-blue ZnSeTe quantum dots through shell engineering toward high color purity light-emitting diodes," Small **19**(45), 2303247 (2023).
[8] A. Liu, C. Bi, J. Li, M. Zhang, C. Cheng, D. Binks, and J. Tian, "High color-purity and efficient pure-blue perovskite light-emitting diodes based on strongly confined monodispersed quantum dots," Nano Lett. **23**(6), 2405–2411 (2023).
[9] T. Otsuka, R. Oka, and T. Hayakawa, "Eu^{3+} site distribution and local distortion of photoluminescent Ca_3WO_6:(Eu^{3+}, K^+) double perovskites as high-color-purity red phosphors," Adv. Sci. **10**(31), 2302559 (2023).
[10] K. Poria, S. Bhatia, R. Kashyap, V. Kashyap, I. Sihmar, N. Deopa, and J. S. Shahi, "Structural and luminescence properties of novel Eu^{3+}-doped $Na_3Ba_2LaNb_{10}O_{30}$

phosphors with high quantum efficiency and excellent color purity for w-LED applications," RSC Adv. **14**, 29490–29504 (2024).
[11]Y. Xiang, Z. Liu, Y. Gao, L. Feng, T. Zhou, M. Liu, Y. Zhao, X. Lai, J. Bi, and D. Gao, "Novel double perovskite $Ca_2Gd_{0.5}Nb_{1-x}W_{5/6}O_6$:0.5 Eu^{3+} red phosphors with excellent thermal stability and high color purity for white LEDs," Chem. Eng. J. **456**, 140901 (2023).
[12]K.-T. Lee, S. Y. Han, Z. Li, H. W. Baac, and H. J. Park, "Flexible high-color-purity structural color filters based on a higher-order optical resonance suppression," Sci. Rep. **9**, 14917 (2019).
[13]Y. Xu, Z. Cheng, Z. Li, B. Liang, J. Wang, J. Wei, Z. Zhang, and Y. Wang, "Molecular-structure and device-configuration optimizations toward highly efficient green electroluminescence with narrowband emission and high color purity," Adv. Opt. Mater. **8**(9), 1902142 (2020).
[14]J. Han, Z. Huang, X. Lv, J. Miao, Y. Qiu, X. Cao, and C. Yang, "Simple molecular design strategy for multiresonance induced TADF emitter: Highly efficient deep blue to blue electroluminescence with high color purity," Adv. Opt. Mater. **10**(4), 2102092 (2022).
[15]Y. Xu, Q. Wang, J. Wei, X. Peng, J. Xue, Z. Wang, S. J. Su, and Y. Wang, "Constructing organic electroluminescent material with very high color purity and efficiency based on polycyclization of the multiple resonance parent core," Angew. Chem., Int. Ed. **61**(30), e202204652 (2022).
[16]M. H. Fang, Z. Bao, W. T. Huang, and R. S. Liu, "Evolutionary generation of phosphor materials and their progress in future applications for light-emitting diodes," Chem. Rev. **122**(13), 11474–11513 (2022).
[17]Z. Yang, Z. Mao, Z. Xie, Y. Zhang, S. Liu, J. Zhao, J. Xu, Z. Chi, and M. P. Aldred, "Recent advances in organic thermally activated delayed fluorescence materials," Chem. Soc. Rev. **46**, 915–1016 (2017).
[18]M. Mamada, M. Hayakawa, J. Ochi, and T. Hatakeyama, "Organoboron-based multiple-resonance emitters: Synthesis, structure–property correlations, and prospects," Chem. Soc. Rev. **53**, 1624–1692 (2024).
[19]F. Liu, Z. Cheng, Y. Jiang, L. Gao, H. Liu, H. Liu, Z. Feng, P. Lu, and W. Yang, "Highly efficient asymmetric multiple resonance thermally activated delayed fluorescence emitter with EQE of 32.8% and extremely low efficiency roll-off," Angew. Chem. **134**(14), e202116927 (2022).
[20]D. Li, M. Li, D. Liu, J. Yang, W. Li, Z. Yang, H. Yuan, S. Jiang, X. Peng, G. X. Yang, W. Xie, W. Qiu, Y. Gan, K. Liu, and S. J. Su, "High-performance narrowband OLED with low efficiency roll-off based on sulfur-incorporated organoboron emitter," Adv. Opt. Mater. **11**(24), 2301084 (2023).
[21]Q. Li, Y. Wu, Q. Yang, S. Wang, S. Shao, and L. Wang, "Selenium-doped polycyclic aromatic hydrocarbon multiresonance emitters with fast reverse intersystem crossing for narrowband blue emission," ACS Appl. Mater. Interfaces **14**, 49995–50003 (2022).
[22]X. Cao, K. Pan, J. Miao, X. Lv, Z. Huang, F. Ni, X. Yin, Y. Wei, and C. Yang, "Manipulating exciton dynamics toward simultaneous high-efficiency narrowband electroluminescence and photon upconversion by a selenium-incorporated multiresonance delayed fluorescence emitter," J. Am. Chem. Soc. **144**(50), 22976–22984 (2022).
[23]W. Ning, H. Wang, S. Gong, C. Zhong, and C. Yang, "Simple sulfone-bridged heterohelicene structure realizes ultraviolet narrowband thermally activated delayed fluorescence, circularly polarized luminescence, and room temperature phosphorescence," Sci. China Chem. **65**(9), 1715–1719 (2022).
[24]Z. Ye, H. Wu, Y. Xu, T. Hua, G. Chen, Z. Chen, X. Yin, M. Huang, K. Xu, X. Song, Z. Huang, X. Lv, J. Miao, X. Cao, and C. Yang, "Deep-blue narrowband hetero[6]helicenes showing circularly polarized thermally activated delayed fluorescence toward high-performance OLEDs," Adv. Mater. **36**(1), 2308314 (2024).
[25]Y. X. Hu, J. Miao, T. Hua, Z. Huang, Y. Qi, Y. Zou, Y. Qiu, H. Xia, H. Liu, X. Cao, and C. Yang, "Efficient selenium-integrated TADF OLEDs with reduced roll-off," Nat. Photonics **16**, 803–810 (2022).
[26]T. Hua, L. Zhan, N. Li, Z. Huang, X. Cao, Z. Xiao, S. Gong, C. Zhou, C. Zhong, and C. Yang, "Heavy-atom effect promotes multi-resonance thermally activated delayed fluorescence," Chem. Eng. J. **426**, 131169 (2021).
[27]I. S. Park, M. Yang, H. Shibata, N. Amanokura, and T. Yasuda, "Achieving ultimate narrowband and ultrapure blue organic light-emitting diodes based on polycyclo-heteraborin multi-resonance delayed-fluorescence emitters," Adv. Mater. **34**(9), 2107951 (2022).
[28]M. Nagata, H. Min, E. Watanabe, H. Fukumoto, Y. Mizuhata, N. Tokitoh, T. Agou, and T. Yasuda, "Fused-nonacyclic multi-resonance delayed fluorescence emitter based on Ladder–Thiaborin exhibiting narrowband sky-blue emission with accelerated reverse intersystem crossing," Angew. Chem., Int. Ed. **60**(37), 20280 (2021).
[29]I. S. Park, H. Min, and T. Yasuda, "Ultrafast triplet–singlet exciton interconversion in narrowband blue organoboron emitters doped with heavy chalcogens," Angew. Chem., Int. Ed. **61**(31), e202205684 (2022).
[30]X. Wu, J. W. Huang, B. K. Su, S. Wang, L. Yuan, W. Q. Zheng, H. Zhang, Y. X. Zheng, W. Zhu, and P. T. Chou, "Fabrication of circularly polarized MR-TADF emitters with asymmetrical peripheral-lock enhancing helical B/N-doped nanographenes," Adv. Mater. **34**(1), 2105080 (2022).
[31]X. Xiong, Y. C. Cheng, K. Wang, J. Yu, and X. H. Zhang, "A comparative study of two multi-resonance TADF analogous materials integrating chalcogen atoms of different periods," Mater. Chem. Front. **7**, 929–936 (2023).
[32]Y. Chang, Y. Wu, X. Wang, W. Li, Q. Yang, S. Wang, S. Shao, and L. Wang, "Boron, sulfur-doped polycyclic aromatic hydrocarbon emitters with multiple-resonance-dominated lowest excited states for efficient narrowband deep-blue emission," Chem. Eng. J. **451**, 138545 (2023).
[33]K. Di, R. Guo, Y. Wang, Y. Lv, H. Su, Q. Zhang, B. Yang, and L. Wang, "Achieving high-performance narrowband blue MR-TADF emitters by suppressing isomer formation and extending π-conjugate skeletons," J. Mater. Chem. C **11**, 6429–6437 (2023).
[34]H. Gao, S. Shen, Y. Qin, G. Liu, T. Gao, X. Dong, Z. Pang, X. Xie, P. Wang, and Y. Wang, "Ultrapure blue thermally activated delayed fluorescence (TADF) emitters based on rigid sulfur/oxygen-bridged triarylboron acceptor: MR TADF and D-A TADF," J. Phys. Chem. Lett. **13**(32), 7561–7567 (2022).
[35]X. F. Luo, H. X. Ni, A. Q. Lv, X. K. Yao, H. L. Ma, and Y. X. Zheng, "High-efficiency and narrowband OLEDs from blue to yellow with ternary boron/nitrogen-based polycyclic heteroaromatic emitters," Adv. Opt. Mater. **10**(16), 2200504 (2022).
[36]J. Jin, S. Wang, H. Jiang, L. Wang, and W. Y. Wong, "Peripheral selenium modification of multi-resonance thermally activated delayed fluorescence molecules for high-performance blue organic light-emitting diodes," Adv. Opt. Mater. **12**, 2302354 (2024).
[37]X. F. Luo, S. Q. Song, X. Wu, C. F. Yip, S. Cai, and Y. X. Zheng, "A chiral spirofluorene-embedded multiple-resonance thermally activated delayed fluorescence emitter for efficient pure-green circularly polarized electroluminescence," Aggregate **5**, e445 (2023).
[38]S. A. Ahmad, J. Eng, and T. J. Penfold, "Rapid predictions of the colour purity of luminescent organic molecules," J. Mater. Chem. C **10**, 4785–4794 (2022).
[39]W. Cai, C. Zhong, and D. Y. Wu, "Achieving high color purity in multi-resonance thermally activated delayed fluorescence emitters through a substitution-driven design strategy," Mater. Chem. Front. **7**(17), 3762 (2023).
[40]X. Xie and A. Troisi, "Identification via virtual screening of emissive molecules with a small exciton-vibration coupling for high color purity and potential large exciton delocalization," J. Phys. Chem. Lett. **14**(17), 4119–4126 (2023).
[41]X. Wang, C. Wang, and S. Yin, "Rapid estimation of fwhm for OLED emission spectra using bond length and bond-order alterations," J. Chem. Theory Comput. **20**(16), 7327–7336 (2024).
[42]W. Cai, C. Zhong, Z. W. Ma, Z. Y. Cai, Y. Qiu, Z. Sajid, and D. Y. Wu, "Machine-learning-assisted performance improvements for multi-resonance thermally activated delayed fluorescence molecules," Phys. Chem. Chem. Phys. **26**(1), 144–152 (2024).
[43]Q. Peng, Y. Yi, Z. Shuai, and J. Shao, "Toward quantitative prediction of molecular fluorescence quantum efficiency: Role of Duschinsky rotation," J. Am. Chem. Soc. **129**(30), 9333–9339 (2007).
[44](a) Z. Shuai, "Thermal vibration correlation function formalism for molecular excited state decay rates," Chin. J. Chem. **38**(11), 1223–1232 (2020); (b) See http://www.momap.net.cn/ for the information about the background, function, core calculation flowchart, and user manual of the MOMAP software.
[45]Z. Shuai and Q. Peng, "Organic light-emitting diodes: Theoretical understanding of highly efficient materials and development of computational methodology," Natl. Sci. Rev. **4**(2), 224–239 (2017).

[46]M. Frisch, G. Trucks, H. Schlegel, G. Scuseria, M. Robb, J. Cheeseman, G. Scalmani, V. Barone, G. Petersson, H. Nakatsuji *et al.*, *Gaussian 16*, Gaussian Inc., Wallingford, CT, 2016.
[47]C. Adamo and V. Barone, "Toward reliable density functional methods without adjustable parameters: The PBE0 model," J. Chem. Phys. **110**, 6158–6170 (1999).
[48]J. Tao, J. P. Perdew, V. N. Staroverov, and G. E. Scuseria, "Climbing the density functional ladder: Nonempirical meta–generalized gradient approximation designed for molecules and solids," Phys. Rev. Lett. **91**(14), 146401 (2003).
[49]J. D. Chai and M. Head-Gordon, "Long-range corrected hybrid density functionals with damped atom–atom dispersion corrections," Phys. Chem. Chem. Phys. **10**(44), 6615–6620 (2008).
[50]A. D. Becke, "Density-functional thermochemistry. III. The role of exact exchange," J. Chem. Phys. **98**, 5648–5652 (1993).
[51]S. Grimme, "Semiempirical GGA-type density functional constructed with a long-range dispersion correction," J. Comput. Chem. **27**(15), 1787–1799 (2006).
[52]S. Grimme, J. Antony, S. Ehrlich, and H. Krieg, "A consistent and accurate *ab initio* parametrization of density functional dispersion correction (DFT-D) for the 94 elements H-Pu," J. Chem. Phys. **132**(15), 154104 (2010).
[53]T. Yanai, D. P. Tew, and N. C. Handy, "A new hybrid exchange–correlation functional using the Coulomb-attenuating method (CAM-B3LYP)," Chem. Phys. Lett. **393**, 51–57 (2004).
[54]W. J. Pietro, M. M. Francl, W. J. Hehre, D. J. DeFrees, J. A. Pople, and J. S. Binkley, "Self-consistent molecular orbital methods. 24. Supplemented small split-valence basis sets for second-row elements," J. Am. Chem. Soc. **104**(19), 5039–5048 (1982).
[55]R. Krishnan, J. S. Binkley, R. Seeger, and J. A. Pople, "Self-consistent molecular orbital methods. XX. A basis set for correlated wave functions," J. Chem. Phys. **72**, 650–654 (1980).
[56]J. Tomasi, B. Mennucci, and R. Cammi, "Quantum mechanical continuum solvation models," Chem. Rev. **105**(8), 2999–3094 (2005).
[57]A. V. Marenich, C. J. Cramer, and D. G. Truhlar, "Universal solvation model based on solute electron density and on a continuum model of the solvent defined by the bulk dielectric constant and atomic surface tensions," J. Phys. Chem. B **113**(18), 6378–6396 (2009).
[58]Y. Shao, Z. Gan, E. Epifanovsky, A. T. B. Gilbert, M. Wormit, J. Kussmann, A. W. Lange, A. Behn, J. Deng, X. Feng *et al.*, "Advances in molecular quantum chemistry contained in the Q-Chem 4 program package," Mol. Phys. **113**(2), 184–215 (2015).
[59]A. Pershin, D. Hall, V. Lemaur, J. C. Sancho-Garcia, L. Muccioli, E. Zysman-Colman, D. Beljonne, and Y. Olivier, "Highly emissive excitons with reduced exchange energy in thermally activated delayed fluorescent molecules," Nat. Commun. **10**, 597 (2019).
[60]F. Weigend and R. Ahlrichs, "Balanced basis sets of split valence, triple zeta valence and quadruple zeta valence quality for H to Rn: Design and assessment of accuracy," Phys. Chem. Chem. Phys. **7**(18), 3297–3305 (2005).
[61]F. Weigend, "Accurate coulomb-fitting basis sets for H to Rn," Phys. Chem. Chem. Phys. **8**(9), 1057–1065 (2006).
[62]X. Chen, S. Deng, W. Zhang, P. Yin, W. Li, and Z. Shuai, "First-principles prediction for phosphorescence spectra of tetradentate platinum(II) complexes with narrow emission width," J. Phys. Chem. A **129**(10), 2493–2509 (2025).
[63]K. Veys, M. H. E. Bousquet, D. Jacquemin, and D. Escudero, "Modeling the fluorescence quantum yields of aromatic compounds: Benchmarking the machinery to compute intersystem crossing rates," J. Chem. Theory Comput. **19**(24), 9344–9357 (2023).
[64]A. Humeniuk, M. Bužančić, J. Hoche, J. Cerezo, R. Mitrić, F. Santoro, and V. Bonačić-Koutecký, "Predicting fluorescence quantum yields for molecules in solution: A critical assessment of the harmonic approximation and the choice of the lineshape function," J. Chem. Phys. **152**(2), 054107 (2020).